TRINAT Summer Project 2011

Optical Pumping of ^{85}Rb using a Microwave Modulated Diode Laser

Author: Daniel Friesen

Supervisor: Dr. John A. Behr

A report submitted in fulfillment of the requirements for the TRIUMF Summer Research Award for the Prairie Region

August 28, 2011

Abstract

In this work we explore the possibility of optically pumping ^{85}Rb by using one frequency stabilized master laser which injection locks a microwave modulated slave laser. This method would greatly simplify optical pumping isotopes of rubidium, such as ^{82}Rb. The main difference between pumping different isotopes of rubidium is the hyperfine ground state splitting. Changing the frequency of the sidebands relative to the carrier frequency would allow us to easily optically pump any isotope we may need to study. It was found that the amplitude ratio of the sidebands depends greatly on which parameters are adjusted. With our primary setup the upper frequency sideband at 3035 MHz was approximately 8% to optically pump ^{85}Rb. The upper frequency sideband at 1550 MHz was approximately 4% to optically pump ^{82}Rb. This ratio can be increased to a desired ratio (such as 10%) by increasing the power of the RF signal that goes into the diode laser.

Acknowledgements

First and foremost, my utmost thanks goes to my supervisor Dr. Behr, for his attentive supervision and patients. For teaching me many valuable techniques in the field of atomic physics. The experience has been indescribable.

Next, I would like to thank the TRINAT group for explaining concepts, and giving me advice on projects like the Student Symposium and this report.

I would like to thank my friends at the University of Manitoba and Argonne National Lab for the evening Skype calls, which were a great stress-relief.

Lastly, I would like to thank TRIUMF for the Summer Research Award which allowed me to have such a great research experience this summer.

Contents

List of Figures

Chapter 1

Introduction

1.1 Diode Laser Modulation

Frequency modulation by injection locking has been done for the purposes of Magneto-Optical Traps (MOT) before [1]. Gould modulated the slave laser and kept the master laser at a specific frequency to be able to injection lock the slave laser. They used this in a double MOT to trap radioactive isotopes. Modulating the non-frequency stabilized slave laser allows for simpler optical configuration since there is no external cavity in the slave laser.

Other groups have trapped atoms by direct microwave modulation [2]. In this case the group used a single diode laser and modulated it up to frequencies of 6.6 GHz to trap ^{87}Rb. They were able to trap up to 85% the number of atoms as that of the conventional method. The problem with modulating a single laser is that this single laser need to be frequency stabilized. This means that the diode laser need an external cavity which will cause an inherent mode structure for the sideband amplitudes. The group adjusted the free-spectral-range cavity to be 3.3 GHz so that the cavity would support sidebands at frequencies around 6.6 GHz.

In this report, we attempt to microwave modulate a slave laser and injection lock with a master laser as described by Gould for the purposes of optical pumping.

1.2 Beta Decay

Parity violation in the weak interaction was first studied by C. S. Wu et al. in 1956 [3]. She studied β decay of polarized ^{60}Co (J=5).

Parity is a mirror-reflectiong of a system. For instance, "right-handed" particles, which have their intrinsic angular momentum projection aligned along their direction of motion, would be "left-handed" under parity. The helicity which describes left and right handed particles is given by

$$h = \frac{\boldsymbol{s} \cdot \boldsymbol{p}}{|s||p|} \tag{1.2.1}$$

Particles with positive helicity are right handed. Particles with negative helicity are left handed. So parity can be simulated by a spin-filp, as the only difference between the right and left handed particles is the direction of their spin relative to that of their linear momentum.

To simulate this parity effect, Wu reversed the magnetic field direction to flip the spin of ^{60}Co. The result showed that the β counting rate was different in the mirror system as compared to the original system, implying that parity was violated.

In this report we try to optically pump ^{85}Rb (I=5/2-) using a microwave modulated diode laser instead of the usual methods. This should be able to be extended to isotopes of rubidium such as ^{82}Rb (I=1+). If we can polarize ^{82}Rb we could perform further β decay studies on this isotope. ^{82}Rb decays into ^{82}Kr (I=0), a neutrino ν, and a $\beta+$. As the total spin has to add up to +1 for conservation of angular momentum, we need the spin projections of both ν and $\beta+$ to be +1/2. Along with the kinematics of the decay we can infer from this that the beta-spin correlation factor, A, should be +1.

$$W(\theta) = 1 + A\frac{v_\beta}{c}cos(\theta) \tag{1.2.2}$$

The $1^+ \rightarrow 0^+$ has a branching ratio of 86.4% [4], so that A would not be perfectly +1 in an experiment. We can observe the direction of the emitted $\beta+$ and since we know that the spin projections have to be +1/2 for both the ν and the $\beta+$ we can deduce that there are no observed right-handed neutrinos so far.

Chapter 2

Theory

2.1 Fine Structure

Alkalis, such as rubidium, are considered "hydrogen-like" since they have a single s-state electron orbiting the nucleus which is surrounded by closed shell electron orbitals. The interaction between the orbital angular momentum of the electron, **L**, and the magnetic moment associated with the electron's spin, **J**, give rise to the fine splitting. This is usually referred to as a spin-orbit interaction. We will consider to two lowest lying transitions of the fine structure. The energy difference between L=0 to L=1 allows for two transitions. The transition for J=1/2 is referred to as the D1 line, and the transition for J=3/2 is referred to as the D2 line. The fine structure Hamiltonian is given by

$$H_{s-o} = \frac{1}{2}\frac{Ze^2}{4\pi\epsilon_0}\frac{g_s}{2m_e^2c^2}\frac{\boldsymbol{L}\cdot\boldsymbol{S}}{r^3} \tag{2.1.1}$$

where g_s is the electron spin g-factor and the factor of 1/2 arises from the Thomas precession which is a relativistic effect of the electron as it orbits the nucleus. The shift in energy due to the spin-orbit interaction is given by [5]

$$E_{s-o} = \frac{\beta}{2}\left(j(j+1) - l(l+1) - s(s+1)\right) \tag{2.1.2}$$

Where β is the spin-orbit constant

$$\beta = \frac{\hbar^2e^2}{2m_e^2c^24\pi\epsilon_0}\frac{1}{(na_0)^3\, l(l+1/2)(l+1)} \tag{2.1.3}$$

Since there is only one valence electron for alkalis, s=1/2 for each l. So the energy splitting for a given j is

$$\Delta E_{s-o} = \frac{\alpha^2 hcR_\infty}{n^3 l(l+1)} \tag{2.1.4}$$

The fine structure splitting for the D1 and D2 lines is shown in Fig. 2.2.

2.2 Hyperfine Structure

A further splitting arises from the interaction between the nucleus and the magnetic and electric fields generated internally. There are two major contributing terms in the Hyperfine Hamiltonian. The magnetic dipole term is due to the interaction between the nuclear magnetic dipole moment, which includes the nuclear spin **I**, and the magnetic field at the center of the nucleus generated from the electron. This term generally dominates the hyperfine splitting since the magnetic field is largest at the nucleus for s-electrons. The second contribution is from the electric quadrupole term. This further contribution is due to the distribution of charge within the atom creating an electric field gradient. The energy of the nuclear electric quadrupole moment in this gradient gives rise to the hyperfine splitting.

The Hyperfine Hamiltonian can be derived starting from classical concepts and written into the quantum mechanical form using the Wigner-Eckart Theorem. We will first start with the electric quadrupole term and then see that the magnetic dipole term can be derived in a very similar fashion.

2.2.1 Electrostatic Multipole Expansion

The electrostatic interaction between the finite sized, charged nucleus, the charged electrons surrounding it and the rest of the nuclei of a many-electron atom is given by the Hamiltonian of the form [6]

$$H_E = \int_{\tau_e} \int_{\tau_n} \frac{\rho_e \rho_n \mathrm{d}\tau_e \mathrm{d}\tau_n}{r} \tag{2.2.1}$$

Where the variables are defined in Figure 2.1. The charge density of the electrons and the nuclear charge density are ρ_e and ρ_n respectively. We assume that r_e is larger than r_n since we do not expect the electronic charges to be more distant than the radius of the nucleus. So we can say that $\frac{r_n}{r_e} < 1$, and rewrite 1/r using the law of cosines. We can then use the binomial expansion to write Eqn. 2.2.1 in the following form

$$\begin{aligned} 1/r &= \left(r_e^2 + r_n^2 - 2 r_e r_n cos\theta_{en}\right)^{-1/2} \\ &= \sum_l \frac{r_n^l}{r_e^{l+1}} P_l(cos\theta_{en}) \end{aligned} \tag{2.2.2}$$

$$H_E = \sum_l H_{E,l} \tag{2.2.3}$$

where we simply substitute Eqn. 2.2.2 into Eqn. 2.2.1. $H_{E,l}$ determines the energy of the interaction to order 2^l. Where, for l=0, the monopole term is determined, l=1

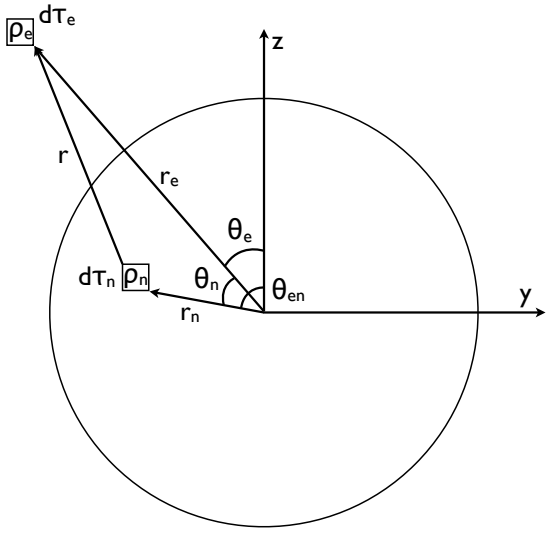

Figure 2.1: Interaction between the nucleus and the electrons of the atom.

corresponds to the electric dipole and l=2, the electric quadrupole term.
We can write the Hamiltonian in terms of irreducible spherical tensors.

$$H_{E,l} = \mathbf{Q^{(l)}} \cdot \mathbf{F^{(l)}} = \sum_{q=-l}^{l} (-1)^q Q_q^{(l)} \cdot F_q^{(l)} \tag{2.2.4}$$

where

$$Q_q^{(l)} = \sqrt{\frac{4\pi}{2l+1}} \int_{\tau_n} \rho_n r_n^l Y_q^l(cos\theta_n, \phi_n) \mathrm{d}\tau_n \tag{2.2.5}$$

and

$$F_q^{(l)} = \sqrt{\frac{4\pi}{2l+1}} \int_{\tau_e} \rho_e r_e^{-(l+1)} Y_q^l(cos\theta_e, \phi_e) \mathrm{d}\tau_e \tag{2.2.6}$$

since

$$P_l(cos\theta_{en}) = \frac{4\pi}{2l+1} \sum_{q=-l}^{l} (-1)^l Y_{-q}^l(cos\theta_n, \phi_n) Y_{+q}^l(cos\theta_e, \phi_e) \tag{2.2.7}$$

The monopole interaction is quite easy to evaluate. We take l=0 which means we only have to evaluate one term for $\mathbf{Q^{(l)}}$ and $\mathbf{F^{(l)}}$.

$$Q_0^{(0)} = \int_{\tau_n} \rho_n \mathrm{d}\tau_n = Ze \tag{2.2.8}$$

$$F_0^{(0)} = \int_{\tau_e} \frac{\rho_e}{r_e} \mathrm{d}\tau_e = \phi^e \tag{2.2.9}$$

which gives us

$$H_{E,0} = Ze\phi^e \tag{2.2.10}$$

Where Z is the atomic number, e is the elementary charge, and ϕ^e is the electrostatic potential at the center of the nucleus due to the electrons outside of the radius of the nucleus. The dipole interaction is similarly easy to evaluate. Here we take l=1 and use the corresponding spherical harmonics to evaluate Eqn. 2.2.5 and 2.2.6. Taking the tensor scalar product between then will give us the dipole interaction.

$$Q_0^{(1)} = \int_{\tau_n} \rho_n z_n \mathrm{d}\tau_n = p_z \tag{2.2.11}$$

$$\pm\, Q_{\pm 1}^{(1)} = \frac{1}{\sqrt{2}} \int_{\tau_n} \rho_n \left(x_n \pm i y_n\right) \mathrm{d}\tau_n = \frac{p_\pm}{\sqrt{2}} \tag{2.2.12}$$

where p_i are the i components of the nuclear electric dipole moment. Next we evaluate the electric field at the center of the nucleus.

$$-F_0^{(1)} = -\int_{\tau_e} \frac{\rho_e}{r_e^3} z \mathrm{d}\tau_e = -\frac{\partial \phi^e}{\partial z} = E_z \tag{2.2.13}$$

$$\pm F_{\pm 1}^{(1)} = -\frac{1}{\sqrt{2}} \int_{\tau_e} \frac{\rho_e}{r_e^3} \left(x \mp i y\right) \mathrm{d}\tau_e = -\frac{1}{\sqrt{2}} \left(\frac{\partial \phi^e}{\partial x} \mp i \frac{\partial \phi^e}{\partial y} \right) = \frac{E_\pm}{\sqrt{2}} \tag{2.2.14}$$

which gives the dipole interaction

$$H_{E,1} = -\mathbf{p} \cdot \mathbf{E} \tag{2.2.15}$$

Only the electric quadrupole term contributes to the hyperfine structure Hamiltonian, so we evaluated l=2 only. Evaluating the tensor components is not very difficult. The difficulty arises when we try to calculate the quantum mechanical expectation values for the quadrupole interaction. It turns we can express the quadrupole moment tensor in terms of quantum mechanical angular momenta. First we calculate the classical term. The $Q_q^{(2)}$ terms are the nuclear electrical quadrupole moment tensor terms.

$$\begin{aligned}
Q_0^{(2)} &= \frac{1}{2} \int_{\tau_n} \rho_n \left(3 z_n^2 - r_n^2\right) \mathrm{d}\tau_n \\
Q_{\pm 1}^{(2)} &= \mp \sqrt{\frac{3}{2}} \int_{\tau_n} \rho_n z_n \left(x_n \pm i y_n\right) \mathrm{d}\tau_n \\
Q_{\pm 2}^{(2)} &= \sqrt{\frac{3}{8}} \int_{\tau_n} \rho_n \left(x_n \pm i y_n\right)^2 \mathrm{d}\tau_n
\end{aligned} \tag{2.2.16}$$

The $F_q^{(2)}$ terms are the gradient terms of the electric field at the center of the nucleus.

$$
\begin{aligned}
F_0^{(2)} = (\nabla E)_0^{(2)} &= \frac{1}{2}\int_{\tau_e} \frac{\rho_e}{r_e^5}\left(3z_e^2 - r_e^2\right) \mathrm{d}\tau_e = -\frac{1}{2}\frac{\partial E_z}{\partial z} \\
F_{\pm 1}^{(2)} = (\nabla E)_{\pm 1}^{(2)} &= \mp\sqrt{\frac{3}{2}}\int_{\tau_e} \frac{\rho_e}{r_e^5} z_e \left(x_e \pm i y_e\right) \mathrm{d}\tau_e = \pm\frac{1}{\sqrt{6}}\left[\frac{\partial E_z}{\partial x} \pm i\frac{\partial E_z}{\partial y}\right] \\
F_{\pm 2}^{(2)} = (\nabla E)_{\pm 2}^{(2)} &= \sqrt{\frac{3}{8}}\int_{\tau_e} \frac{\rho_e}{r_e^5} \left(x_e \pm i y_e\right)^2 \mathrm{d}\tau_e \\
&= -\frac{1}{2\sqrt{6}}\left[\left(\frac{\partial E_x}{\partial x} - \frac{\partial E_y}{\partial y}\right) \pm i\left(\frac{\partial E_y}{\partial x} + \frac{\partial E_x}{\partial y}\right)\right]
\end{aligned} \tag{2.2.17}
$$

Here we have expanded the tensor in terms of the Cartesian components. We can write the terms more generally.

$$
Q_{ij} = \int_{\tau_n} \rho_n \left(3x_{ni}x_{nj} - \delta_{ij} r_n^2\right) \mathrm{d}\tau_n \tag{2.2.18}
$$

$$
(\nabla E)_{ij} = -\int_{\tau_e} \frac{\rho_e}{r_e^5}\left(3x_{ei}x_{ej} - \delta_{ij} r_e^2\right) \mathrm{d}\tau_e \tag{2.2.19}
$$

Then we can write the Hamiltonian describing the electric quadrupole moment interaction as

$$
H_{E,2} = -\frac{1}{6}\sum_{i=x,y,z}\sum_{j=x,y,z} Q_{ij}\left(\nabla E\right)_{ij} \tag{2.2.20}
$$

This is easy to show explicitly by simply multiplying the terms in Eqn. 2.2.4 where the terms for $Q_q^{(2)}$ and $F_q^{(2)}$ are given on the previous page.

This quadrupole moment tensor can be written in terms of angular momentum using a theorem describe by Ramsey [7]. This theorem is valid for tensors that undergo space rotations in the same manner as the spherical harmonics. In particular. The tensor needs to have the same dependence on the magnetic quantum number m as does the nuclear spin I. The theorem allows us to write a simple proportionality for Eqn's 2.2.16 and the angular momentum variables.

$$
\begin{aligned}
Q_0 &= \frac{C}{2}\left(3I_z^2 - \mathbf{I^2}\right) \\
Q_{\pm 1}^{(2)} &= \mp\sqrt{\frac{3}{2}}\frac{C}{2}\left(I_z I_\pm + I_\pm I_z\right) \\
Q_{\pm 2}^{(2)} &= \sqrt{\frac{3}{8}} C I_\pm^2
\end{aligned} \tag{2.2.21}
$$

where the constant C is given by evaluating the quadrupole moment Q.

$$
C = \frac{Qe}{I(2I-1)} \tag{2.2.22}
$$

In a similar manner we can write the tensor components of the electric field gradient in terms of the angular momentum **J**, since the orientation of the atom is specified by it. Again we can relate Eqn's 2.2.17 to the total angular momentum through a gradient dependent term q_J.

$$
\begin{aligned}
(\nabla E)^{(2)}_0 &= \frac{eq_J}{2J(2J-1)}\left(3J_z^2 - J(J+1)\right) \\
(\nabla E)^{(2)}_{\pm 1} &= \mp\frac{\sqrt{6}}{2}\frac{eq_J}{2J(2J-1)}\left(J_z J_\pm + J_\pm J_z\right) \\
(\nabla E)^{(2)}_{\pm 2} &= \frac{\sqrt{6}}{2}\frac{eq_J}{2J(2J-1)}J_\pm^2
\end{aligned}
\tag{2.2.23}
$$

where q_J can be related to the electric field gradient

$$
q_J = \frac{1}{e}\left\langle \frac{\partial^2 V^e}{\partial z^2} \right\rangle_{JJ} \tag{2.2.24}
$$

Now we can compute the sum of Eqn. 2.2.20 to get the electric quadrupole term of the hyperfine structure Hamiltonian.

$$
H_{E,2} = \frac{e^2 q_J Q}{2I(2I-1)J(2J-1)}\left[3(\boldsymbol{I}\cdot\boldsymbol{J})^2 + 3/2\boldsymbol{I}\cdot\boldsymbol{J} - I(I+1)J(J+1)\right] \tag{2.2.25}
$$

The quadrupole energy is

$$
E_{E,2} = \frac{B_{HFS}}{8I(2I-1)J(2J-1)}\left[3K(K+1) - 3I(I+1)J(J+1)\right] \tag{2.2.26}
$$

where B_{HFS} is related to the spectroscopic quadrupole moment and the electric field gradient due to the distribution of charges within the atom

$$
B_{HFS} = e\left\langle \frac{\partial^2 V^e}{\partial z^2} \right\rangle_{JJ} Q \tag{2.2.27}
$$

and where K contains contributions from the total angular momentum term from the atom, **F**, the nuclear spin, **I**, and the total angular momentum of the electron, **J**.

$$
\mathbf{K} = \mathbf{F^2} - \mathbf{I^2} - \mathbf{J^2} \tag{2.2.28}
$$

2.2.2 Magnetic Multipole Expansion

In a similar manner as above we can write down the Hamiltonian of the magnetic dipole term classically. We consider the electrons with current density $\mathbf{j_e}$ producing a vector potential $\mathbf{A_e}$ at the nucleus. This current interacts with the nuclear density current $\mathbf{j_n}$ and the Hamiltonian can be written as

$$H_M = -\frac{\mu_0}{4\pi}\int_{\tau_n} \mathbf{j_n}\cdot\mathbf{A_e}\mathrm{d}\tau_\mathbf{n} \tag{2.2.29}$$

The nuclear current density can be derived from the vector potential $\mathbf{m_n}$

$$\mathbf{j_n} = \frac{\mathbf{4}\pi}{\mu_\mathbf{0}}\nabla\times\mathbf{m_n} \tag{2.2.30}$$

Using this relation, it can be shown that if a surface S_n surrounds the nucleus but lies just outside of it

$$H_M = -\int_{\tau_n} \mathbf{m_n}\cdot\mathbf{H_e}\mathrm{d}\tau_\mathbf{n} \tag{2.2.31}$$

where H_e is the magnetizing field. We consider the contribution that is due to the electron currents only.

$$\mathbf{H_e^e} = \nabla_\mathbf{n}\times\mathbf{A_e^e} = \nabla_\mathbf{n}\int_{\tau_\mathbf{n}}\frac{\nabla_\mathbf{e}\cdot\mathbf{m_e}}{\mathbf{r}}\mathrm{d}\tau_\mathbf{e} \tag{2.2.32}$$

The above equation should not be immediately obvious as we need various vector relations to come up with the above equality. We also need to consider that $\mathbf{m_e}$ vanishes over the inner surface which defines the electron-current distribution and the outer surface to the electron distribution. The Hamiltonian can now be written as

$$H_M^e = \int_{\tau_e}\int_{\tau_n}\frac{(-\nabla_n\cdot\mathbf{m_n})(-\nabla_\mathbf{e}\cdot\mathbf{m_e})}{r}\mathrm{d}\tau_e\mathrm{d}\tau_n \tag{2.2.33}$$

This is very similar to Eqn. 2.2.1 and so we can use the same theorem as for the the electrostatic multipole expansion. Specifically, Eqn. 2.2.11 can be used to write an expression for the nuclear magnetic dipole moment by noting the similarities in the two Hamiltonians. They can be related by $\rho_n \to -\nabla_n\cdot\mathbf{m_n}$ so that with the help of vector identities

$$\boldsymbol{\mu_I} = \int_{\tau_n}(-\nabla_n\cdot\mathbf{m_n})\mathbf{r_n}\mathrm{d}\tau_\mathbf{n} = \int_{\tau_\mathbf{n}}\mathbf{m_n}\mathrm{d}\tau_\mathbf{n} \tag{2.2.34}$$

The magnetic dipole Hamiltonian can then be quickly written down by drawing analogy from Eqn. 2.2.15

$$H_{M,1} = -\boldsymbol{\mu_I}\cdot\mathbf{B_e} \tag{2.2.35}$$

where $\mathbf{B_e}$ is the magnetic field due to the orbiting electron. This magnetic field is given by [8]

$$\boldsymbol{B_e} = \frac{\mu_0}{4\pi}\left[-\frac{8\pi}{3}\boldsymbol{\mu_e}\delta(\boldsymbol{r}) + \frac{1}{r^3}\left[\boldsymbol{\mu_e}\cdot\boldsymbol{\mu_n} - 3\frac{(\boldsymbol{\mu_e}\cdot\boldsymbol{r})\boldsymbol{r}}{r^2} - \frac{e}{m}\boldsymbol{L}\right]\right] \tag{2.2.36}$$

where $\boldsymbol{\mu_e} = -g_s\mu_B\boldsymbol{S}$ and we take $g_s = 2$. For $L = 0$ only the first term prevails, while for $L \neq 0$ the first term vanishes and we evaluate the last term. Also considering the

form of the magnetic moment of the nucleus will show that for the hyperfine structure we consider a IJ coupling, opposed to the LS coupling seen in the fine structure. The electron energies which are also defined by the total angular momentum $\boldsymbol{J}$ lead to a splitting which is a couple of orders of magnitude smaller than the fine splitting. The nuclear magnetic moment is proportional to its angular momentum, mainly the nuclear spin

$$\boldsymbol{\mu_I} = \frac{\mu_I}{I}\boldsymbol{I} \tag{2.2.37}$$

So we can write Eqn. 2.2.35 as

$$\begin{aligned} H_{M,1} &= A_{HFS}\boldsymbol{I}\cdot\boldsymbol{J} \\ E_{M,1} &= A_{HFS}\left[F(F+1) - I(I+1) - J(J+1)\right] \end{aligned} \tag{2.2.38}$$

where A_{HFS} is the hyperfine A constant defined as follows

$$A_{HFS} = \left(\frac{2\mu_o\mu_B\mu_I}{4\pi I}\right)\frac{8\pi}{3}|\psi(0)|^2 \qquad L = 0 \tag{2.2.39}$$

$$A_{HFS} = \left(\frac{2\mu_o\mu_B\mu_I}{4\pi I}\right)\left\langle\frac{1}{r^3}\right\rangle\frac{L(L+1)}{J(J+1)} \qquad L \neq 0 \tag{2.2.40}$$

For L=0 we call the magnetic dipole term the Fermi contact interaction since it depends on the the square of the wavefunction.

2.3 Hyperfine structure of ^{85}Rb

The first two terms, the magnetic dipole term and the electric quadrupole term, of the hyperfine Hamiltonian are now fully described. The energy due to the hyperfine structure is given by

$$\begin{aligned} E_{HFS} = A_{HFS}&\left[F(F+1) - I(I+1) - J(J+1)\right] \\ &+\frac{B_{HFS}}{8I(2I-1)J(2J-1)}\left[3K(K+1) - 3I(I+1)J(J+1)\right] \end{aligned} \tag{2.3.1}$$

The energy levels for ^{85}Rb for the L=0 and L=1 electron states are shown in Fig. 2.2. It should be noted that the nuclear spin of ^{85}Rb is I=5/2 that of ^{87}Rb is I=3/2 and that or ^{82}Rb is I=1. The frequency shifts from the D1 and D2 lines, in reference to ^{87}Rb, are shown in Table 2.3 The data used to obtain these values for both the table and the figure is taken from [9]. A Table for the ^{82}Rb transition frequencies is also shown below using the data from [10]. This information will be useful when discussing Optical Pumping, which we will do next, and will be referred to back as needed. Before moving on, we note that the ground state splitting in ^{85}Rb is 3035MHz and that of ^{82}Rb is approximately 1550MHz. The error in the transition frequencies was also obtained from [10] by propagation.

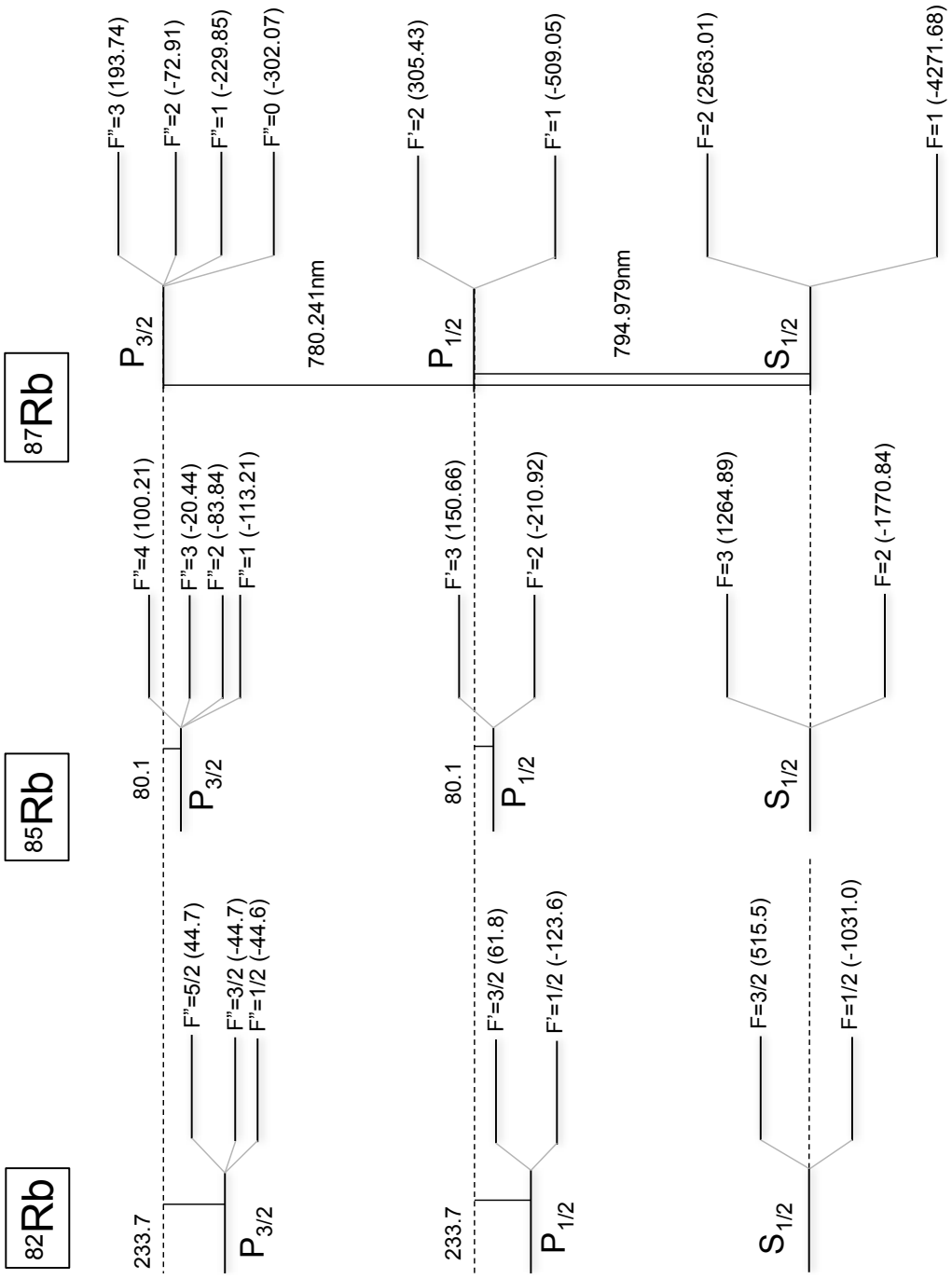

Figure 2.2: Energy levels of ^{82}Rb and ^{85}Rb in reference to ^{87}Rb. All splitting are indicated in units of Hertz.

F → F"	MHz	F → F'	MHz
3 → 4"	-1244.78	3 → 3'	-1194.23
3 → 3"	-1365.43	3 → 2'	-1555.91
3 → 2"	-1428.83		
2 → 3"	1670.30	2 → 3'	1841.40
2 → 2"	1606.90	2 → 2'	1479.82
2 → 1"	1577.53		

Table 2.1: Frequency shifts from the D1 and D2 lines to drive the specific transitions in ^{85}Rb

F → F"	MHz	F → F'	MHz
3/2 → 5/2"	-705(3)	3/2 → 3/2'	-688(2)
3/2 → 3/2"	-794(4)	3/2 → 1/2'	-873(2)
3/2 → 1/2"	-793(4)		
1/2 → 3/2"	753(5)	1/2 → 3/2'	859(2)
1/2 → 1/2"	752(5)	1/2 → 3/2'	674(2)

Table 2.2: Frequency shifts from the D1 and D2 lines to drive the specific transitions in ^{82}Rb

2.4 Optical Pumping

Optical Pumping is a technique that polarizes atoms in a specific state. There are different reasons as to why we would want to do this, one of which is described in the Introduction. We already mentioned that Rubidium, an alkali, has one valence electron which simplifies the optical pumping scheme quite a bit. The electron's final M value cannot differ by more than one from it's initial M value. By conservation of angular momentum, if we shine right circularly polarized light which carries momentum $\hbar$ along it's direction of propagation, we will excite a ΔM_F transition of $+1$, or $+\sigma$. Left circularly polarized light carries momentum -$\hbar$ along it's direction of propagation and excites a ΔM_F transition of -1, or -σ, where $\Delta M_F = M'_F - M_F$. Shining right circularly polarized light of the right frequency will lift an electron out of the $4^2S_{1/2}$ state and excite it into the $4^2P_{1/2}$ state as shown in Fig. 2.3.

When a small magnetic field is applied the F spectral lines split into their projections, m_F. This is due to the weak field Zeeman effect. These states are more or less equally populated since the spacing is much less than k_BT. Let's assume we have now exited the atom as shown in Fig. 2.3. Once the atoms are in the excited state they will undergo emission, which on average would be $\Delta M_F = 0$. Repeated absorption and emission will cause a "random biased walk" where the atom will eventually occupy the highest M_F value in the ground state, specifically $F = 3, M_F = 3$. Now the atom is polarized, which could in principle be measured. We cannot pump the atom any further since there is no other M_F state which would be satisfied by shining

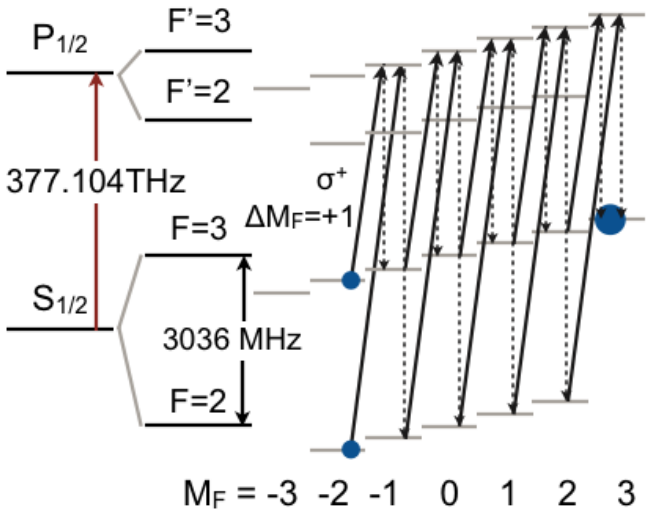

Figure 2.3: Optical Pumping scheme of ^{85}Rb.

$+\sigma$ light onto the atom. The gas is now said to be transparent to the photons. This decrease, and eventually the absence of absorption can be observed by looking at a fluorescence signal.

We could imagine a setup of $+\sigma$ light shining into a glass cell filled with rubidium vapour and a photodetector. A magnetic field would be applied over the glass cell. The signal on the photodetector would be at a maximum when the gas is polarized, hence it is called transparent.

This process of optical pumping to polarize the atoms is usually done with two lasers. One would pump the $2 \rightarrow 3'$ transition and the other would drive the $3 \rightarrow 3'$ transition. We do not necessarily need to use two lasers and instead could use acousto-optic modulators (AOM) or electro-optic modulators (EOM). AOM's can be used when the ground state hyperfine splitting isn't very large. In ^{85}Rb the splitting is roughly 3035 MHz which is too large for an AOM. EOM's can modulate the laser light in the gigahertz but are quite expensive. The use of a Mini-Circuits Voltage Controlled Oscillator (VCO) can simplify this optical pumping scheme by modulating the laser light in the gigahertz and these parts are also relatively cheap.

2.5 Magneto-Optical Trap

A way of confining cold, neutral atoms is with the Magneto-Optical Trap (MOT). Shown in Fig. 2.4 are three counter-propagating laser beams and a quadrupole field produced by coils arranged in the anti-Helmholtz configuration. The coils cancel out, so that the magnetic field at the origin is zero. Near the origin is a uniform field gradient that varies the energy levels of the atom linearly with the atoms position.

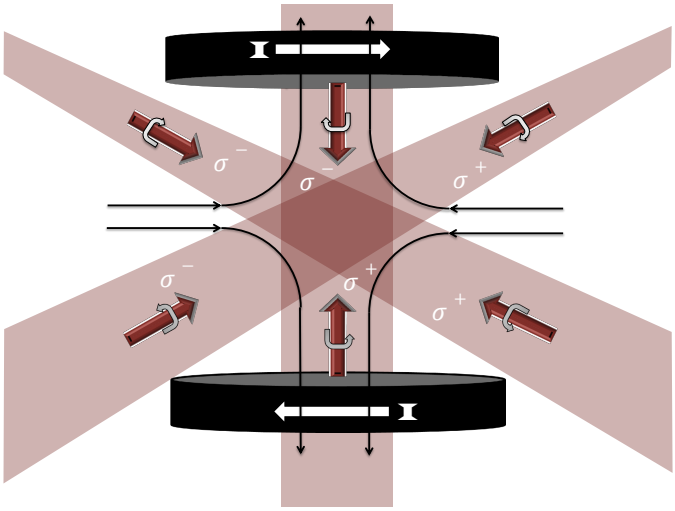

Figure 2.4: Magneto-Optical Trap setup. Three counter-propagating laser beams and anti-Helmholtz coils which produce a quadrupole field.

This is shown in Fig. 2.5 for the most basic $J = 0$ to $J = 1$ transition. The counter-propagating beams are circularly-polarized. If the atoms are not in the centre these beams produce an imbalance in the radiative force that ultimately pushes the atoms into the centre of the trap. Photons that are right-circularly polarized, denoted by $+\sigma$, have momentum $\hbar k$, where k is the wavenumber, and thus excite a $\Delta M_J = +1$ transition. This is due to conservation of momentum. The atom which absorbs the photon is given a momentum kick which is the same direction as the photons momentum. In order to actually trap the atoms we need to tune the laser light a few linewidths below the resonant frequency [11], or to the red. Light of this nature will push the atoms towards the centre since atoms will see the light Doppler shifted closer to resonance and opposing the motion of the atoms. Left-circularly polarized light, or $-\sigma$ will excite a $\Delta M_J = -1$ transition since this kind of photon carries momentum $-\hbar k$ along it's direction of propagation. We assume that the atom is now in the $i > 0$ region of Fig. 2.5, where i is the horizontal axis along the B field. In this case the $\Delta M_J = -1$ transition progresses closer to resonance with the laser frequency. Since the laser frequency is to the red it gives a damping force due to optical molasses.

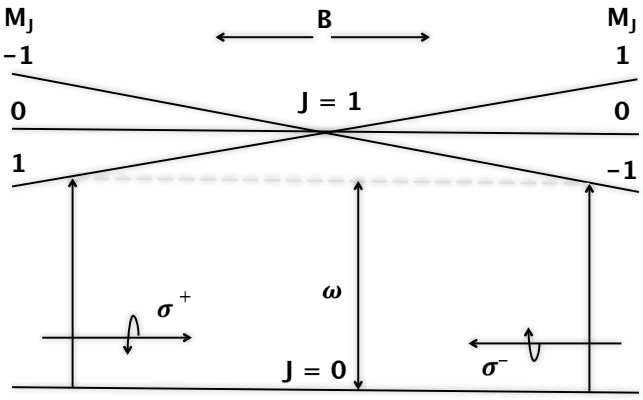

Figure 2.5: The Magneto-Optical Trap mechanism for a transition of $J = 0$ to $J = 1$. The selection rules between the Zeeman states show an imbalance in the radiate forces of the laser beams. When the radiative forces are balanced in all direction, the atoms will accumulate in the centre of the trap.

2.5.1 Optical Molasses

In order to reduce the temperature of atoms that are moving in all directions as a gas, they need to be laser cooled in all three directions. The three orthogonal counter-propagating beams, shown in Fig. 2.4, create standing waves. The radiative forces only balance each other for stationary atoms and push moving atoms towards the centre of the trap. If we are in the reference frame of a moving atom which is moving towards the right as illustrated in Fig. 2.6 the red beam is Doppler shifted and brings the light closer to resonance with the moving atom. Due to this effect, the atom absorbs more light from this beam and the beam slows down the atom. This can be shown mathematically [5]

$$\begin{aligned} F_{molasses} &= F_{scatt}(\delta - kv) - F_{scatt}(\delta + kv) \\ &\approx -2\frac{\partial F}{\partial \delta}kv = -\alpha v. \end{aligned} \tag{2.5.1}$$

Hence the resultant force is proportional to the negative of the atoms velocity. Where in Eqn. 2.5.1 low velocities have been assumed. This force can be used to describes a viscous fluid and is hence called molasses. Here $\delta = \omega - \omega_0$, where ω_0 is the resonant frequency and ω is the laser frequency shifted, is slightly to the red. The damping

coefficient can be written as

$$\alpha = 4\hbar k^2 \frac{I}{I_{sat}} \frac{-2\delta/\Gamma}{[1+(2\delta/\Gamma)^2]^2} \tag{2.5.2}$$

where Γ is the linewidth of the the laser beam. We can see form Eqn. 2.5.1 that the

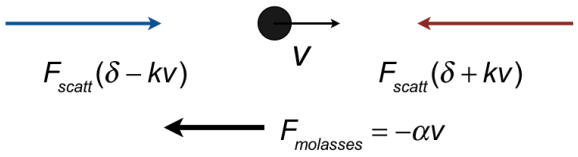

Figure 2.6: Optical Molasses is a laser cooling technique that involves three counter-propagating laser beams that are orthogonal to each other. The laser beams are slightly red shifted with frequency ω. Moving atoms experience the Doppler effect and scatter of light propagating in the opposite direction of the atoms motion. An imbalance in the forces dampens the atoms motion, and the atoms are stationary when the radiative forces are balanced.

process of damping requires a positive values of α and so we need that $\delta = \omega - \omega_0 < 0$, hence red-detuned.

Chapter 3

Experimental Techniques

3.1 Microwave Modulation Setup

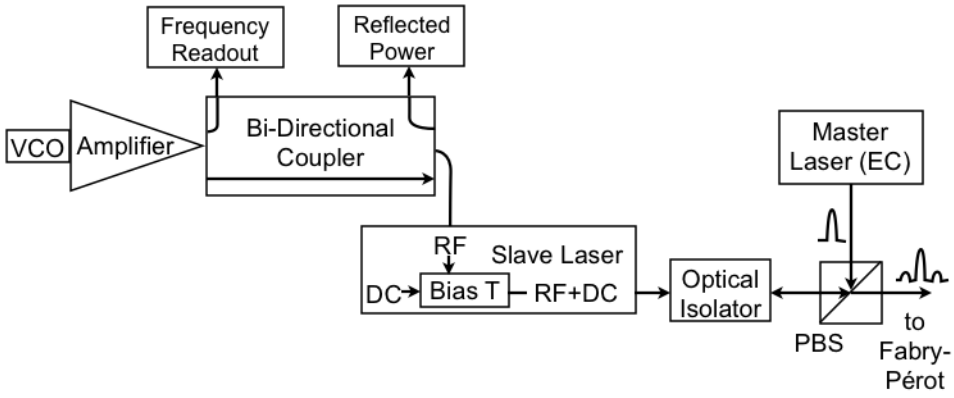

Figure 3.1: Setup for modulating the carrier frequency of the slave laser, injection locked by the master laser.

The actual process of frequency modulating the diode laser (putting sidebands on the laser) was done as shown in the setup of Fig. 3.1. The diode laser used was a Toptica DC 110. The parts used to send an RF signal into the Bias Tee, included with the laser, where Mini-Circuits parts. The Voltage Controlled Oscillator (VCO) generates sinusoidal waveforms that are controlled in oscillation frequency by a DC input. This is called the Tune Voltage, and can be varied to give different frequency sidebands. In this report we measured the amplitude of these sidebands form a frequency range of approximately 800-3200 MHz. To attain this frequency range we required three different VCO's. The first one [12] (ZX95-1600W-S+) has a frequency range from 800-1600 MHz and a power output of +9dBm. The next model (ZX95-2600+) has a frequency range from 1650-2600 MHz and a power output of +6dBm.

The last model used (ZX95-3250-S+) has a frequency range from 2550-3250 MHz and a typical power output of +2dBm. To keep the output power at approximately 24 ± 2 mW, the input voltage (VCC) into the VCO was adjusted.

Next comes an amplifies (ZJL-5G) which has a typical gain of 9dB and works over the entire interest of frequencies, particularly from 20-5000 MHz. Two bi-directional couplers were used. The first model (ZABDC20-182H-S+) operates for frequencies between 700-1800 MHz. The second model (ZABDC20-322H-S+) operates between 1700-3200 MHz. The coupler was used to monitor the frequency of the sidebands and the reflected power. It was also used to calibrate the power, so that we know how many mW we are sending into the diode laser. The power was readout using a power detector (ZX47-40LN-S+) which operators over all frequencies of interest for this particular experiment.

Lastly, this setup was hooked up to the diode laser via a bias tee (ZFBT-4R2G-FT+) which was also operational over the frequencies of interest. A DC signal is given to the "slave laser" by adjusting the current to 78mA and the temperature of the laser to 18.3°C for the desired wavelength. The RF signal comes from the VCO using the setup described above. The slave laser is injection locked by a frequency stabilized "master laser". This injection locking[1] transfers the narrow line width and spectral stability to the slave laser. This process also allows us to only frequency stabilize one laser instead of two lasers. Hence the process of optical pumping requires less work, as locking a laser requires careful consideration of a number of parameters.

The now modulated carrier frequency goes to a Fabry Pérot to measure the percent power that is in the sidebands, relative to the carrier frequency. The Fabry Pérot also allows us to make sure that the sidebands are at the right frequency as readout by the frequency counter. Before making these measurements, we first made sure that the master laser is frequency stabilized by looking at the Saturation Absorption signal.

3.2 Fabry Pérot

The Fabry Pérot consists of two highly reflective mirrors and a piezo-electric transducer on one of the mirrors. Driving the piezo-electric transducer with a ramp voltage scans the distance between the two mirrors. Once the distance between the two mir-

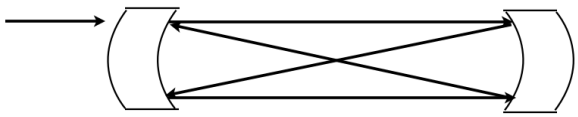

Figure 3.2: Light entering from the left into a pair of highly-reflected mirrors. It then follows a figure-eight path, undergoing four path length before exiting into a photo-diode.

rors, d, supports constructive interference light will exit the two mirror arrangement and produce a transmission peak. For destructive interference, no transmission is observed. The distance between two such transmission peaks is called the Free Spectral Range (FSR) given by

$$\Delta\lambda = \frac{c}{4d} \tag{3.2.1}$$

The FSR divided by the Full Width at Half Maximum (FWHM), $\delta\lambda$, of the transmission peak gives the finesse [13], F, of the apparatus.

$$F = \frac{\Delta\lambda}{\delta\lambda} \approx \frac{\pi R^{1/2}}{1-R} \tag{3.2.2}$$

where R is the reflectivity of the mirrors, assuming it is the same for both. Below we show a sample spectrum as seen on the Fabry Pérot at 1000 MHz sidebands. To measure how much percent amplitude is in the sidebands relative to the carrier amplitude we take a ratio of the sideband amplitude to the carrier amplitude. To get the ratios between the frequencies of 800-3200 MHz we used a 10 GHz Fabry Pérot (Thorlabs SA210) and a 30 GHz one. We could have only used the 10 GHz Fabry-Perot to get the required ratios.

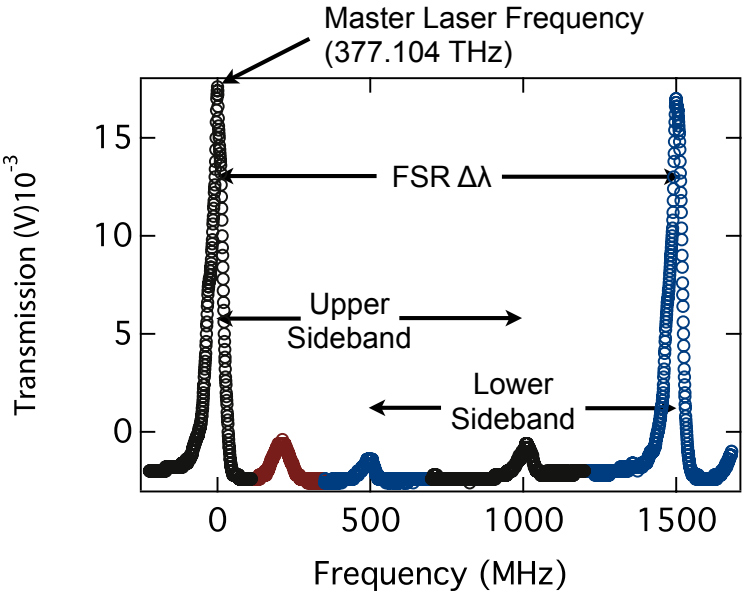

Figure 3.3: Sample spectra of the 1000 MHz sidebands. The black shows the upper sideband and the blue shows the lower frequency sideband. The red is the slave laser carrier frequency which we try to minimize.

3.3 Saturation Absorption Spectroscopy

3.3.1 Unsaturated Signal

In order to look at the hyperfine structure of 85Rb, a saturated absorption signal is needed. The setup to get such a signal is shown in Fig. 3.4. Rubidium vapour fills the cell where atoms are moving with a Maxwell-Boltzmann probability distribution, $P(v_i)$, of velocities

$$P(v_i) \propto e^{\frac{-mv_i^2}{2kT}} \tag{3.3.1}$$

where k is the Boltzmann constant, T is the absolute temperature, and m is the particles mass. Atoms with a velocity class of

$$v_i = c\left(\frac{\nu_T}{\nu_L} - 1\right) \tag{3.3.2}$$

where ν_T is the transition frequency and ν_L is the laser frequency, will interact with the weak probe beam. This is because the Doppler shifted frequency is given by

$$\nu' = \nu_L\left(\frac{v_i}{c} + 1\right) \tag{3.3.3}$$

It is easy to see that if we plug Eqn. 3.3.2 into Eqn. 3.3.3 the transition frequency is equal to the Doppler shifted frequency.

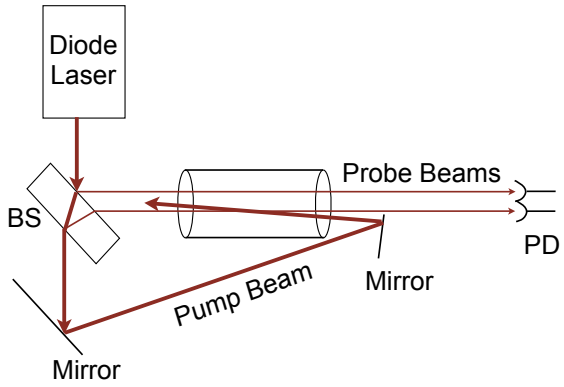

Figure 3.4: Setup of Saturation Absorption Spectroscopy. The Rubidium vapour cell is in the centre of the schematic. The abbreviation are: Glass Plate Beam Splitter (BS) and Photo-diode (PD).

When the transition frequency is greater than the laser frequency, $\nu_T > \nu_L$, v_i is positive and the atoms moving towards the laser beam will absorb light. The top

photo-diode signal in Fig. 3.4 would give a Gaussian shaped signal since the probe beam will successively interact with all velocity classes. In other words, the Doppler broadened, or unsaturated probe beam, signal is due to fast moving atoms.

3.3.2 Saturated Signal

The bottom photo-diode signal gives a saturated probe beam spectrum. Here we have a strong pump beam and a weak probe beam crossing inside the rubidium vapour cell. The velocity class centred about $v_i = 0$ will interact with both beams. The strong pump beam will excite a great fraction of the atoms so that there are less atoms in the ground state for the weak probe beam to interact with. Hence less atoms in the ground state absorb light from the probe beam and the absorption signal is decreased.

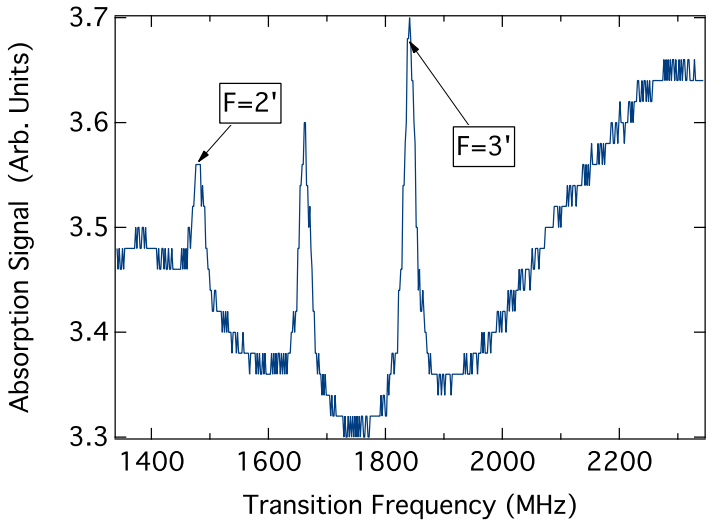

Figure 3.5: Partially subtracted Doppler free signal for the ^{85}Rb F=2 to 2' and 3' transitions. The crossover peak is not labelled and is between the two hyperfine transitions.

Another way of looking at it, is to consider the situation when $\nu_T > \nu_L$. The negative velocity class, $-v_i$ as given by Eqn. 3.3.2 will partially absorb the pump beam. At the same time the positive velocity class, v_i, is partially absorbed by the probe beam. This is because the two laser beams are travelling in opposite directions so they interact with velocity classes of opposite sign. Since these velocity classes are completely different, the absorption signal for the probe beam is not affected. On the other hand, if the transition and laser frequency are equal to each other, $\nu_T = \nu_L$, both beams absorb the same velocity class. Mainly the velocity class centred about $v_i = 0$. Since the strength of the two beams is not equal, the probe beams absorption

signal is decreased since less atoms are in the ground state due to their absorption of the pump beam.

A subtraction of the top from bottom photo-diode, or unsaturated minus saturated probe beam, signal leads to a spectrum that should ideally just show the peaks corresponding to the hyperfine transitions. The spectrum in Fig. 3.5 shows a partially subtracted signal with the transitions labeled.

3.3.3 Crossover Peak

The D1 line allows two transitions for the $F = 2$ hyperfine state. Yet Fig. 3.5 shows three peaks which, as described in the previous section, correspond to transitions. The middle peak is called a crossover peak and does not correspond to a physical transition.

This peak can be understood by assuming that the laser frequency ν_L is now exactly half way between the $F = 2 \rightarrow 2'$ and $F = 2 \rightarrow 3'$ transitions during it's scan. These transitions have a common lower state, $F = 2$. Again, since the pump beam is travelling in the opposite direction as the probe beam, it interacts with the negative velocity class now given by

$$v_i = -c\left(\frac{\nu_{2\rightarrow 2'}}{\nu_L} - 1\right) \tag{3.3.4}$$

where $\nu_{2\rightarrow 2'}$ is the transition frequency for $F = 2 \rightarrow 2'$. This same velocity class also seems the probe beam shifted to drive the $F = 2 \rightarrow 3'$ transition. There are now less atoms in the gourd state for the weak probe beam to excite and we once again see a peak in the spectrum.

It is worth mentioning that emission of a photon leads to dips in the signal seen in Fig. 3.5. This can also be due to transitions having a common upper state instead of the above mentioned common lower state. The pump beam can excite atoms with a given velocity class from a lower state to a common upper state and the atoms then decay into both ground states. The probe beam excites atoms of the same velocity class in the second lower state to the common upper state. This is an example of optical pumping increasing the population of the lower state and leads to an increased absorption signal. When subtracted, the Doppler free signal will show a dip.

3.3.4 Saturation Absorption Signal with Sidebands

A Saturation Absorption signal was also taken with the modulated beam. The setup was as in Fig. 3.4. The diode laser was now frequency modulated and the spectra are shown in figure below. The spectra show emission as well as some absorption, but the emission is quite a bit stronger. Where we see the emission signal being to the left and absorption to the right in Fig. 3.6 b), this is reversed after we pass 3035MHz, which would be required for optical pumping. The saturation signal with 3035 MHz sidebands does not show any structure. This is not completely understood.

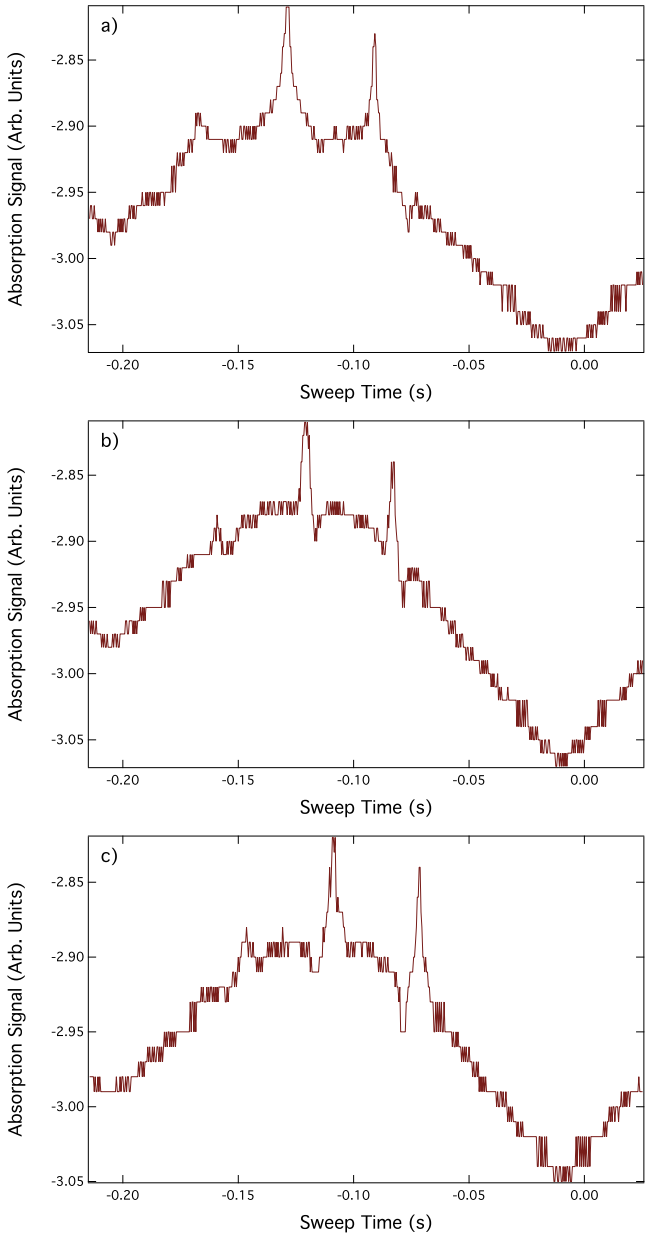

Figure 3.6: Saturation Absorption Spectroscopy signal where the beam (as shown in Fig. 3.4) has upper and lower frequency sidebands at a) 2900 MHz b) 3000 MHz and c) 3100 MHz. In all spectra we see an absorption and emission signal. This is not entirely understood.

Chapter 4

Experimental Results

4.1 Amplitude Ratio of Sidebands

4.1.1 Suppression of Slave Laser

The amplitude of the sidebands and the carrier peaks were measured of similar spectra to that of Fig. 3.3. Voigt functions were fit to each of the peaks using Igor Pro's Multipeak function. The error used was taken from the uncertainty in the parameter values. The slave lasers carrier peak was 4nm away from the master lasers carrier peak. Also since the slave laser was injection locked by the master laser we should only have observed the master laser peak.

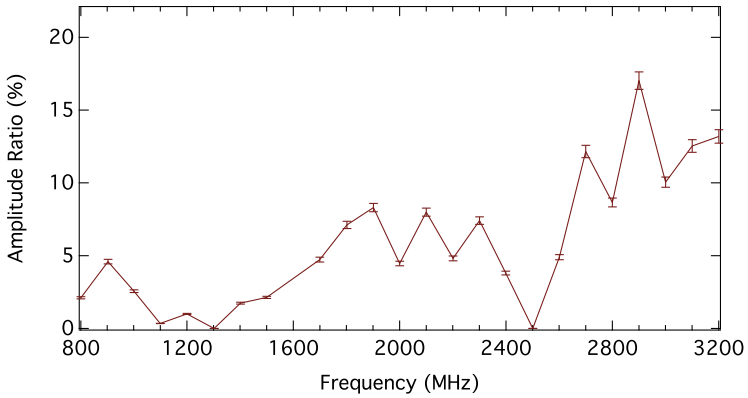

Figure 4.1: The slave laser carrier frequency amplitude relative to the master laser carrier frequency amplitude. The slave laser amplitude is suppressed as best as possible for each frequency.

A small slave laser peak was observed which most likely arose from the optic arrangement in Fig. 3.1 not being ideal. As a result the amplitude of the slave

laser peak was suppressed by slightly adjusting the current going into the slave laser. We see that the slave lasers carrier peak was easier to suppress at lower frequencies compared to the higher frequencies after 2500 MHz. The percent amplitude in the slave laser didn't exceed 15% and since it is also 4nm away from the master frequency it should not interfere with the optical pumping.

4.1.2 Measurement of Sidebands Amplitude

As described above, the amplitude of the upper and lower frequency sidebands are determined by fitting Voigt functions to the Fabry-Perot signals and dividing these by the amplitude of the carrier peak. The error associated with each parameter are propagated by quadrature to get the final error in the amplitude ratio. The amplitude ratio is shown in Fig. 4.2 below. The optical pumping scheme for ^{85}Rb is shown in Fig. 2.3 and if we want to do it by frequency modulation, we need sidebands at 3036 MHz. Specifically the upper frequency sideband would drive the $F = 3 \rightarrow 3'$ transition. For this frequency the upper frequency sideband is approximately 8% of the carrier amplitude. This should be enough to optically pump ^{85}Rb. To pump ^{82}Rb the upper frequency sideband need to be around 1550 MHz. Here we see the amplitude ratio is only about 4%. This may not be enough to optically pump ^{82}Rb.

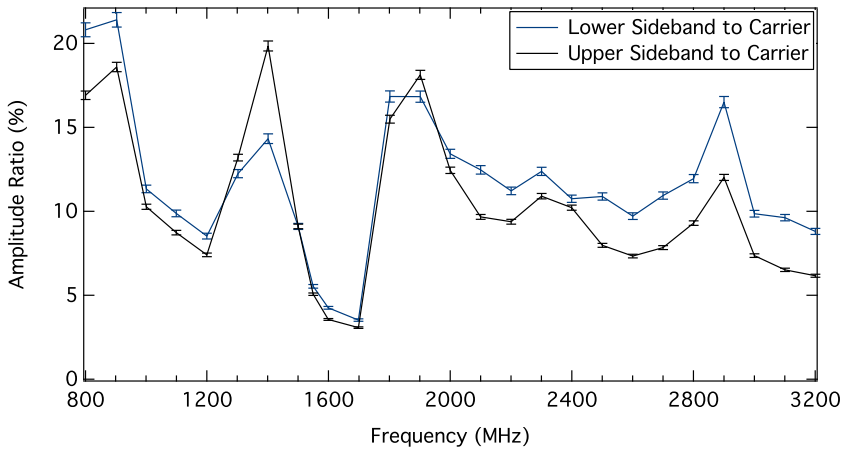

Figure 4.2: Percent Amplitude in the Upper (black) and Lower (blue) frequency sidebands relative to the master carrier peak. The two particular areas of interest are around 3036 MHz, to optically pump ^{85}Rb, and around 1550 MHz, to optically pump ^{82}Rb.

Another thing we see by inspecting Fig. 4.2 is that the lower sideband is generally a few precent larger in amplitude than the upper frequency sideband. This is especially easy to see at frequencies above 2000 MHz. This is caused by a superposition of AM

and FM modulation[14]. This can be shown mathematically by describing a optical wave which is simultaneously FM and AM modulated.

$$E = E_0 \left[1 + Mcos(2\pi f_m t)\right] exp\left[i(2\pi f_0 t + \beta sin(2\pi f_m t))\right] \tag{4.1.1}$$

where M is the amplitude modulation index, f is the instantaneous frequency, f_m is the modulated frequency, and β is the frequency modulation index.

We could expand Eqn. 4.1.1 in terms of spherical Bessel functions which would then show that the upper sideband has a larger amplitude than the lower sideband if the FM and AM are in phase. The lower sideband has a larger amplitude than the upper sideband if the FM and AM are out of phase. The AM modulation arises when the laser is above the lasing threshold. The slope of power versus excitation increases drastically and increasing the current input into the laser increases the amplitude of the beam. One source of FM is form simply changing the input into the VCO and changing the frequency of the sidebands. Also by changing the current that goes into the laser we change the number of the electrons in the conduction band of the crystal, which changes its index of refraction. This ultimately changes the frequency of the carrier peak. Another way of changing it, is by moving the grating since the diode laser is in the Littrow configuration.

Another quick observation we can make form Fig. 4.2 is that there may be an apparent mode structure in the setup. We see "spikes" in the amplitude ratio about every 500 MHz starting at 900 MHz.

4.1.3 Reflected Power in Setup

The reflected power was readout as shown in Fig. 3.1 and is shown below as a function of frequency (Fig. 4.3). We see that the structure follows approximately that of Fig. 4.2. There are two obvious spikes at 2400 and 1900 MHz that coincide with that of Fig. 4.2. This is most likely due to some sort of mode structure in the setup. The actual connection between the bi-directional coupler and the bias tee was made with a BNC connection where the Mini-Circuits parts prefer SMA connections. The BNC connectors are usually used for frequencies below 3 GHz whereas SMA connectors can be used for frequencies up to 18 GHz. This could be a cause of the mode structure in the setup.

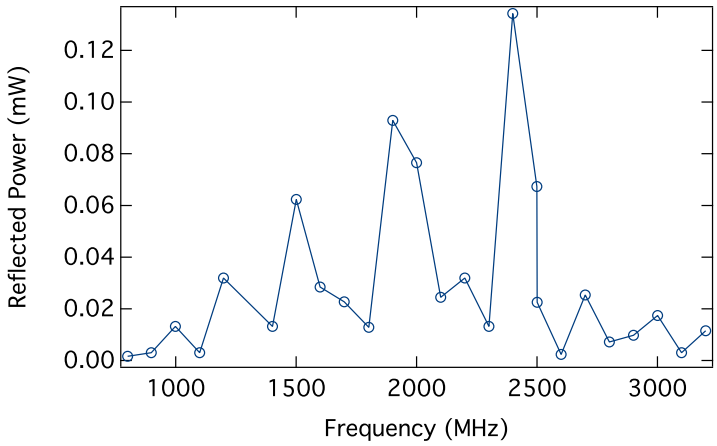

Figure 4.3: Reflected Power readout as shown in Fig. 3.1.

4.1.4 Increasing Power of Sidebands

In Fig. 4.2 we observed that the amplitude ratio at 1550 MHz was only about 4%, which may not be enough to optically pump ^{82}Rb. We would like the ratio to be not less than 10%. A way of increasing the power in the sidebands is by increasing the Vcc.

Using the VCO model ZX95-1600W-S+ we checked how the sideband ratio increased as the input voltage into the VCO was increased. At maximum Vcc the VCO performs with optimal output power as described by the manufacture.

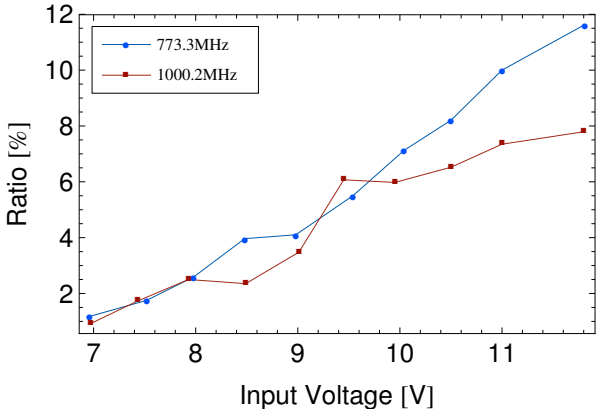

Figure 4.4: The ratio of the sidebands can be increased by increasing the input voltage (Vcc) into the VCO(without amplifier in setup). For this test we used the model ZX95-1600W-S+ which can have a maximum Vcc of 12V.

For instance, to get the amplitude ratio up to 10% at 1550 MHz we can increase

the Vcc into the VCO to 8.31V where it maximally takes 12V. The input voltage into the VCO was kept at 7.80V for the data shown in Fig. 4.2. At 7.80V we were within the 24 ± 2 mW, and at 8.31V into the VCO the output power was approximately 32 mW. The input voltage into the VCO cannot just be increased arbitrarily to get the amplitude ratio in the sidebands that is desired. We need to make sure that the power of the RF signal that is sent into the bias tee is below the DC power of the actual laser.

4.2 Preparation of Optical Pumping

The rubidium MOT in the TRINAT lab is a double MOT. The first part to check before optical pumping, is how the number of atoms trapped scales with the re-pumper power. We want to see how many radioactives we loose if the re-pumper is cut down. Particularly, we want to chop down the re-pumper in the first MOT as we push the atoms with a blue detuned push beam into the second MOT. We see a similar trend as to Fig. 4.5 as we attenuate the re-pumper beam in the first MOT.

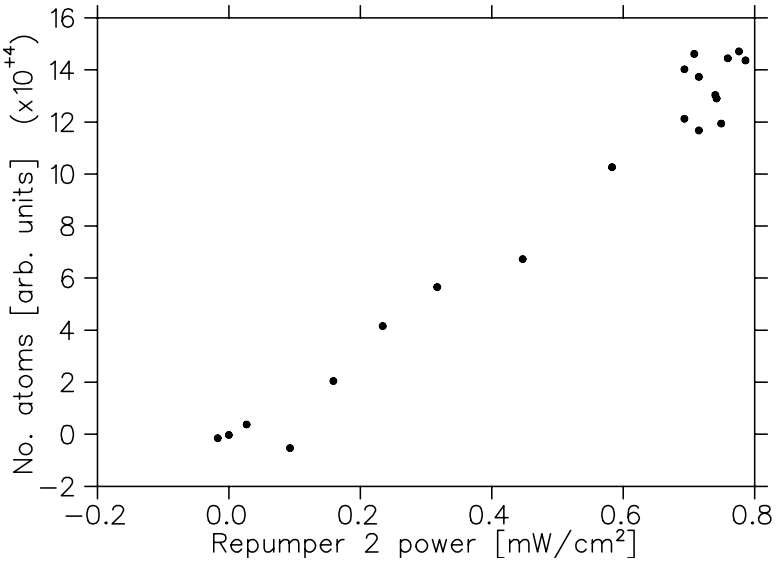

Figure 4.5: The number of atoms trapped is proportional to the re-pumper power in the second MOT. A similar relation is seen in the first MOT.

Chapter 5

Conclusion

In this report we explored a way of simplifying optical pumping for different isotopes of rubidium. Frequency modulation of a slave laser which is injection locked by a frequency stabilized can shorten the time for setting up an optical pumping scheme. This requires a saturation absorption spectroscopy, so that we know which transition to lock the master laser to, and a Fabry Pérot setup to check the frequency and amplitude of the sidebands.

The goal was to have the amplitude ratio of the sidebands to be relatively independent of the frequency so that we could quickly change the frequency of the sidebands to pump another, different isotope of rubidium. The amplitude of the sidebands can be easily adjusted by increasing the Vcc into the VCO or by getting a bigger amplifier. The amplitude of the sidebands should not be increased arbitrarily, as we need to make sure that the power of the RF does not exceed that of the DC into the slave laser.

We did not test the actual optical pumping of ^{85}Rb, but the ratio of the upper frequency sideband suggested that the optical pumping should work. To polarize ^{82}Rb we may have to increase the input voltage into the VCO, which we were safely able to do, without damaging the diode laser.

Bibliography

[1] R. Kowalski and S. Root and S. D. Gensemer and P. L. Gould, *A frequency-modulated injection-locked diode laser for two-frequency generation* AIP. **72**, 6, 2532-2534, (2001). 1, 18

[2] C. J. Myatt and N. R. Newbury and C. E. Wieman, *Simplified atom trap by using direct microwave modulation of a diode laser*, Opt. Lett., **18**, 8, 649-651, (1993). 1

[3] C. S. Wu, E. Ambler, R. W. Hayward, D. D. Hoppes, and R.P. Hudson, *Experimental Test of Parity Conservation in Beta Decay*, Phys. Rev., **105**, 1413-1415, (1957). 1

[4] Crane, S. G. and Brice, S. J. and Goldschmidt, A. and Guckert, R. and Hime, A. and Kitten, J. J. and Vieira, D. J. and Zhao, X., *Parity Violation Observed in the Beta Decay of Magnetically Trapped* ^{82}*Rb Atoms*, Phys. Rev. Lett., **86**, 14, 2967-2970, (2001). 2

[5] C.J. Foot, *Atomic Physics*, Oxford University Press, (2005). 3, 15

[6] N. Ramsey, *Molecular Beams*, Oxford University Press, (1956). 4

[7] N. Ramsey, *Nuclear Moments*, John Wiley and Sons, (1953). 7

[8] G.K. Woodgate., *Elementary Atomic Structure, 3rd ed.*, Clarendon Press, (1980). 9

[9] Daniel A. Steck, *Rubidium 85 D Line Data*, available online at http://steck.us/alkalidata (revision 2.1.4,23 December 2010). 10

[10] Thibault, C. and Touchard, F. and Büttgenbach, S. and Klapisch, R. and de Saint Simon, M. and Duong, H. T. and Jacquinot, P. and Juncar, P. and Liberman, S. and Pillet, P. and Pinard, J. and Vialle, J. L. and Pesnelle, A. and Huber, G. *Hyperfine structure and isotope shift of the D2 line of Rb76-98 and some of their isomers*, Phys. Rev. C. **23**, 6, 2720-2729, (1981). 10

[11] J A Behr and G Gwinner, *Standard model tests with trapped radioactive atoms*, J. Phys. G. **36**, 3, 033101, (2009). 14

[12] *Mini-Circuits Webpage*, http://www.minicircuits.com, Viewed 22 August 2011. 17

[13] G. Brooker, *Modern Classical Optics*, Oxford University Press, (2003). 19

[14] Kobayashi, S. and Yamamoto, Y. and Ito, M. and Kimura, T., *Direct frequency modulation in AlGaAs semiconductor lasers*, IEEE J. Quantum Electron., **18**, 4, 582-595, (1982). 26